INTERNATIONAL JOURNAL FOR NUMERICAL METHODS IN FLUIDS
Int. J. Numer. Meth. Fluids 2004; **44**:927–956 (DOI: 10.1002/fld.658)

Pressure weighted upwinding for flow induced force predictions: application to iced surfaces

G. F. Naterer*,†,‡

University of Manitoba, Winnipeg, Manitoba, Canada R3T 2N2

SUMMARY

This paper addresses two main topics, namely the development of a pressure-weighted upwinding method and its application to flow induced forces on iced cylinders. Although the near-wall convective upwinding exhibits special applicability to iced surfaces, its capabilities extend more generally to other applications. By fully linking pressure and velocity at a sub-element level near the wall, a higher order accuracy can be obtained. Also, a non-physical de-coupling between pressure and velocity can be prevented. The method is developed under the context of a control-volume-based finite element method for 2-D, incompressible flows. Drag and lift coefficients are predicted, based on the pressure weighted upwinding near the wall. The numerical predictions are successfully compared against experimental data, including flow induced forces on iced cables. © 2004 John Wiley & Sons, Ltd.

KEY WORDS: upwinding; flow-induced forces; CFD: convection modelling; control-volume based finite element method

1. INTRODUCTION

Accurate predictionm of flow induced forces on objects, such as iced power lines or aircraft surfaces, is an important concern for design purposes. For example, dynamic forces caused by icing of overhead power lines can lead to large financial losses associated with various hardware damage, and possibly human injury and death due to interruption of a power supply. Although lighter icing occurs more frequently than extreme icing, the shape of a lightly iced cable may cause it to behave like an airfoil in a side wind. The resulting aerodynamic loads may produce unstable flow-induced line vibrations (called galloping), whereby the resulting dynamic line and tower forces become much greater than forces produced by the static ice weight alone. These flow-induced scenarios are recognized in the Canadian Electrical Code [1],

*Correspondence to: G. F. Naterer, Department of Mechanical and Industrial Engineering, University of Manitoba, 15 Gillson Street, Winnipeg, Manitoba, Canada R3T 2N2.
†E-mail: natererg@cc.umanitoba.ca
‡Associate Professor.

Contract/grant sponsor: Manitoba Hydro
Contract/grant sponsor: Natural Sciences and Engineering Research Council of Canada

Received 14 May 2003
Revised 16 September 2003

but detailed variations due to changing ice shape are not well understood. The purpose of this article is to consider a pressure based convective upwinding in the near-wall region, for more accurate predictions of the flow induced forces on a surface.

In recent decades, the rapid progress of CFD (Computational Fluid Dynamics) has provided an effective design tool for engineering problems, particularly in problems where experimental testing is too time-consuming or expensive. Numerical methods for CFD are typically based on finite elements [2] finite volumes [3] or combined elements/volumes [4]. Complete geometric flexibility is achieved with finite elements, thereby allowing unstructured grids and local elemental equations to be developed independently of the mesh configuration. Galerkin weighted residuals may be used in deriving these discrete equations [5]. In the case of finite volume methods, balances of conserved quantities over discrete volumes are applied.

Interpolation methods for predicting the convective fluxes at the edges of these volumes, such as exponential and upwind differencing, have been described by Patankar [3]. Schneider and Raw [6, FIELDS] extend single variable interpolations to coupled pressure/velocity fields at the midpoint of the volume edges. In PAC (physical advection correction), a correction term is added to the upstream value predicted by UDS, in order to improve the upwinding accuracy. A grid upstream scheme with PAC is documented by Wong and Raithby [7]. Van Doormaal *et al.* [8] suggest that numerical oscillations can arise with PAC in grid upstream schemes when advection terms are dominant, due to large variations of the advective components of the PAC term. Furthermore, Lillington [9] has documented the need to include the effect of the local pressure gradient in the evaluation of the PAC correction term.

In physical influence schemes (PINS) [10], a methodology of incorporating the Second Law locally is considered, particularly so that upstream differencing in the convection modelling complies with the Second Law. This methodology represents extensions of FIELDS to accommodate the requirements imposed by the Second Law in the upstream differencing. Convergence acceleration with higher order accuracy of the upstream interpolation is documented by Leonard [11], based on a method called QUICK. Hutchinson and Raithby [12] outline a multigrid algorithm for convergence acceleration, whereby coarse and fine grids are used together to reduce the discretization errors. These methods of reducing solution errors, particularly involving convection, have special significance when predicting more complex phenomena such as multiphase flows with droplets, icing and phase change. Such examples involving aircraft icing are documented by Cebeci *et al.* [13], Hedde and Guffond [14] and Shin *et al.* [15].

An important application where CFD can provide useful insight is external flows, such as flows past overhead power lines. In this example, numerical simulations can be used to predict the wind forces on the power line, in addition to ice loads arising from atmospheric icing. Although CFD technology serves as a key tool in the aerodynamics of aircraft design, less attention has been given to its potential benefits in power transmission applications. Various differences distinguish the needs of power line icing calculations from other methods, thereby requiring special consideration of the near-wall convection modelling. For example, power line icing usually occurs during freezing precipitation with relatively large droplets (up to 1 mm diameter) and low wind speeds (up to about 10 m/s). However, aircraft icing typically entails much smaller droplets (about 10–30 μm) and higher air speeds (usually above 45 m/s). Larger droplets impart more latent energy across the convective boundary layer when freezing on impact. Also, lower air speeds have less inertia (relative to the droplets) when deflecting droplets away from the ice surface before impact. Since many aspects of the icing predictions

depend on the near-wall convection modelling, the method of convective upwinding with sub-element pressure/velocity links has large significance in icing problems.

Fluid dynamics and computational predictions of flows past bluff bodies, such as cylinder type bodies, have been widely studied in the technical literature. At sufficiently low air velocities past a circular cylinder, the boundary layer remains laminar [16]. Delayed separation of the boundary layer from the surface occurs at higher Reynolds numbers [17], i.e. $Re > 3 \times 10^5$ (where $\mathrm{Re} = VD/v$ and V, D and v refer to the air velocity, diameter and kinematic viscosity of air, respectively). Flow induced vibrations, due to time varying lift coefficients, further alter the structure of vortex shedding in the downstream wake [18].

When predicting such fluid motion, conventional error estimation is often based on Taylor series methods [5]. Naterer and Rinn [19] develop a useful alternative to these conventional error indicators using a weighted entropy residual. This method overcomes certain difficulties of Taylor series methods, particularly involving evaluation of higher order derivatives and constants in the error indicators. Reducing solution errors in the near-wall velocity and pressure distributions has significance when predicting the drag and lift forces on the object. The fluid/structure interactions are derived from these forces. In this article, the fluid and structure will refer to the air flow and cable (uniced and iced), respectively, although the method is more generally applicable to other geometries and applications.

Despite many past fluid dynamic studies involving circular cylinders, a wide variety of other cylinder type configurations, such as D-shaped cylinders, has received less attention. These configurations can occur during certain conditions of atmospheric icing of overhead power lines. In particular, elliptical, D-shaped and other oval type conductor shapes are encountered due to surface icing. Numerical simulations with CFD offer a useful tool for better understanding of flow induced forces on these types of surfaces. For example, they can shed new light on flow conditions leading to vibration galloping [20], when CFD includes the detailed effects of multiphase flow, impinging droplets and ice buildup on cables. Such vibrations are derived by forces involving shear stress and pressure calculations along the surface. Once calculated, these distributions are integrated around the iced surface to determine the aerodynamic force coefficient (i.e. c_d or c_l).

Although previous studies have modelled the surface shear stress analytically (i.e. Ref. [21]), extensions to more complex shapes of iced cables by CFD are investigated in this article. Unlike various past schemes for convective upwinding (i.e. UDS, EDS [3]), the current method links pressure with convective velocities at a sub-element level. Benefits of this approach are discussed in this article, particularly how they relate to the accuracy of the predicted flow induced forces on the surface. For example, higher order accuracy can be derived by pressure weighted upwinding, while retaining a physically based coupling between velocity and pressure. Furthermore, wind tunnel testing is used to gather experimental data for physical understanding and validation of the finite element studies. It is anticipated that these studies can provide useful new information regarding drag and lift forces due to ice buildup on surfaces. Although the application problems investigate iced cables, the numerical method can be applied to other iced surfaces, such as iced aircraft surfaces.

2. PROBLEM FORMULATION

The problem formulation involves a description of the governing equations, and discretization of the solution domain and governing equations.

2.1. Governing equations

The general 2-D conservation equation for a scalar quantity, ϕ, may be written as

$$\rho \frac{\partial \phi}{\partial t} + \rho \frac{\partial (\phi u)}{\partial x} + \rho \frac{\partial (\phi v)}{\partial y} + \frac{\partial (j_x)}{\partial x} + \frac{\partial (j_y)}{\partial y} = \rho \hat{S} \tag{1}$$

where j_x, j_y and $\hat{S}$ refer to the diffusive flux components and source term, respectively. In the case of momentum transport, the diffusive flux vector, **j**, refers to stress tensor (including pressure), whereas it refers to the heat flux in the case of energy transport. In the mass and momentum equations for an incompressible Newtonian fluid (such as air), the following continuity and Navier–Stokes equations are obtained:

$$\frac{\partial u}{\partial x} + \frac{\partial v}{\partial y} = 0 \tag{2}$$

$$\rho \frac{\partial u}{\partial t} + \rho \frac{\partial (uu)}{\partial x} + \rho \frac{\partial (uv)}{\partial y} = -\frac{\partial p}{\partial x} + \mu \left(\frac{\partial^2 u}{\partial x^2} + \frac{\partial^2 u}{\partial y^2} \right) \tag{3}$$

$$\rho \frac{\partial v}{\partial t} + \rho \frac{\partial (vu)}{\partial x} + \rho \frac{\partial (vv)}{\partial y} = -\frac{\partial p}{\partial y} + \mu \left(\frac{\partial^2 v}{\partial x^2} + \frac{\partial^2 v}{\partial y^2} \right) \tag{4}$$

where $\mathbf{v} = (u, v)$ is the velocity field, μ is the dynamic viscosity and p is the kinematic pressure. After appropriate initial and boundary conditions are specified, Equations (2)–(4) can be solved to find the velocity and pressure fields. In icing problems, simultaneous predictions of ice growth involve the heat transfer and multiphase flow equations [22].

2.2. Numerical discretization

The numerical solution requires discretization of the problem domain, as well as the governing equations. In this section, the method of spatial discretization is based on a CVFEM (control-volume-based finite element method). The CVFEM combines the geometric flexibility of the finite element method with the important conservation based properties (i.e. enforcement of mass, energy conservation) of the finite volume procedure. In the upcoming sections, the benefits of this method in regards to sub-element convective modelling will be described, particularly its role in predicting the flow induced forces on a surface.

The solution domain is sub-divided into an assembly of quadrilateral isoparametric elements. Each finite element is further subdivided into a set of sub-control-volumes (SCVs; see Figure 1). Then, after assembly of all elements, a finite volume is established by all sub-volumes associated with a particular node. Local co-ordinates, s and t, are used within each element. Integration points (ip) are defined at the midpoint of each sub-surface (SS) in order to evaluate the surface flux terms, such as the mass or momentum flux, in the control volume equations.

Then, bilinear shape functions are used for global/local co-ordinate transformations and the interpolation of scalar values in the domain. For example, the value of a general scalar

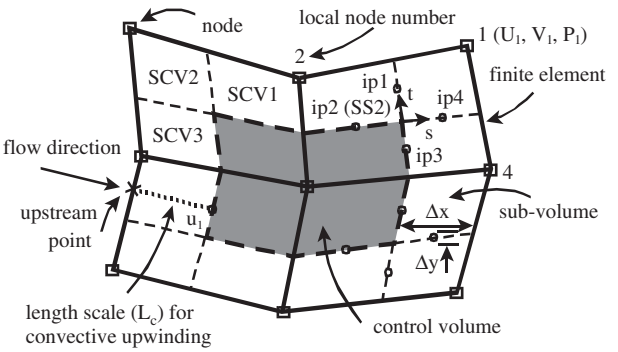

Figure 1. Finite element/volume discretization with sub-element interpolation.

quantity, ϕ, at the local co-ordinate, (s,t), is approximated by

$$\phi(s,t) = \sum_{i=1}^{4} N_i(s,t)\Phi_i \tag{5}$$

where the shape functions, N_i, are given by

$$\begin{aligned} N_1(s,t) &= \tfrac{1}{4}(1+s)(1+t) \\ N_2(s,t) &= \tfrac{1}{4}(1-s)(1+t) \\ N_3(s,t) &= \tfrac{1}{4}(1-s)(1-t) \\ N_4(s,t) &= \tfrac{1}{4}(1+s)(1-t) \end{aligned} \tag{6}$$

The subscripts $i = 1,2,3$ and 4 refer to local nodes. Based on these shape functions, all interpolated values of the scalar and their derivatives may be obtained. In Equation (5), it should be noted that t refers to the local co-ordinate outlined in Figure 1, not time.

The discrete form of the governing equations may be obtained by integration of the general scalar conservation equation, i.e. Equation (1), over a discrete volume, with the result that

$$\int_A \frac{\partial(\rho\phi)}{\partial t}\,\mathrm{d}A + \int_S (\rho\phi\mathbf{v})\cdot\mathbf{dn}\Big|^{n+1} + \int_S \mathbf{j}\cdot\mathbf{dn}\Big|^{n+1} = \int_A \rho\hat{S}\,\mathrm{d}A\Big|^{n+1} \tag{7}$$

where **dn** is the unit normal vector. Also, integrations over A and S refer to the area and surface of the 2-D control volume, respectively. An implicit formulation is adopted, whereby the convection, diffusion and source terms are evaluated at the current time level (denoted by superscript $n+1$), rather than the previous time level (superscript n; explicit approach).

Linearization of the convection and source terms is required in Equation (7). Velocities at the previous iteration, or previous time step values before the first iteration at the beginning of a new time step, are used in this regard. These velocities are called the 'linearized' or 'lagged' velocities. A combination of the newly solved velocity and the value from the previous

iteration at a given node is used, based on a relaxation factor of 0.5. Similarly, values from the previous iteration with a lumped approximation are used for linearization of the source term on the right side of Equation (7). In the lumped approximation, a piecewise constant distribution based on the nodal value is used to find the spatially averaged source term. Also, a backward difference in time is used when approximating the first term of Equation (7). The diffusive flux, **j**, is typically expressed in terms of the gradient of the scalar (i.e. Fourier's Law), so bilinear interpolation with the shape functions can be used for discretizing the third term in Equation (7).

With reference to SCV1 (see Figure 1), the convective term in Equation (7) will require evaluation at both SS1 and SS4 sub-surfaces since both surfaces contribute to the convective transport of ϕ for the SCV1 conservation equation. In the case of the SS1 evaluation, we have

$$\int_{SS1} (\rho\phi\mathbf{v}) \cdot \mathbf{dn} \approx (\rho\phi u)_{\mathrm{ip1}}^{n+1} \Delta y_1 - (\rho\phi v)_{\mathrm{ip1}}^{n+1} \Delta x_1 \tag{8}$$

The values Δx_1 and Δy_1 refer to lengths associated with SS1 (see Figure 1). A similar expression is obtained for the SS4 integration. As mentioned previously, the superscript $n+1$ in Equation (8) refers to the current time step.

Since an implicit formulation is used, inter-equation iterations involving the conservation equations for mass and momentum (i.e. $\phi = u$ or v) are required to handle the non-linear convective term in Equation (8). For example, in the momentum equation, the convective term in Equation (8) involves a 'convected' (linearized or lagged) velocity multiplied by a 'convecting' velocity (to be discussed hereafter). The sub-iteration strategy first solves the flow equations based on the linearized velocities, and then compares the newly predicted velocities with the convected velocities in the linearized convection terms. Unless the summed difference between these velocities over the problem domain falls below a specified convergence tolerance (non-dimensional value of 0.001 in the current study), the convected velocity is updated and the procedure is repeated. Otherwise, the results are considered to be convergent and the solution can proceed to the next time step. When the convected velocity is updated, a relaxation factor of 0.5 is applied, so that an equal combination of newly predicted and previously linearized velocities are used in the next iteration.

Initial and boundary conditions are required for closure of the formulation. In particular, boundary conditions for velocity and pressure are required. The velocity components may be specified at inlets, outlets and walls. However, outlet flow conditions may be unknown in certain cases. If little or no streamwise changes in velocity are expected in such cases, then a zero gradient of velocity can be imposed at the outlet boundary. In these cases, the momentum equations at boundary nodes are replaced by the velocity specifications. Furthermore, the velocity conditions are used for calculating boundary mass flows in the closure of the boundary control volume equations for mass conservation. If the flow rate or expected velocity gradients at the boundaries are unknown, but the pressure drop across the domain is known, then pressure boundary conditions can be applied. The continuity equation is replaced by such pressure conditions. Pressure boundary conditions are particularly useful in internal flows, such as problems with flows exiting the domain at more than one location. In any case, at least one reference pressure must be specified at a node within the domain, in order to ensure a unique solution of the momentum equations.

For example, consider the numerical implementation of boundary conditions for an external flow past an iced conductor. This article focuses on this type of problem. Sufficient distance from the outlet and top/bottom edges of the domain to the conductor are required for zero gradient conditions on those boundaries. The momentum equations are replaced by conditions specifying that the boundary velocities are equal to their adjacent nodal values perpendicular to the boundary nodes. The control volume equations for mass conservation at the boundary nodes are completed after adding the mass outflows. The outlet condition could be imposed so that any errors in this specification will not propagate upstream. A zero streamwise gradient is often mild enough to permit the computations to proceed, although subsequent refinements in the grid layout may be required to establish that the solution results are independent of the outlet location and boundary conditions. At the inlet and conductor boundaries, specified velocity conditions are applied. In this case, the momentum equations are replaced by fixed values of velocity, while the known mass fluxes are used for closure of the control volume equations for mass conservation.

3. NUMERICAL FORMULATION OF FLOW INDUCED FORCES

In this section, the method of calculating the flow induced forces, as well as its pressure based upwinding and order accuracy, will be described.

3.1. Computation of drag and lift coefficients

After the solutions of the Navier–Stokes equations are obtained, the aerodynamic forces and coefficients (c_d, c_l) are often needed. In two-dimensional problems, the wall shear stress for Newtonian fluids is obtained from the following constitutive relation:

$$\tau_{xy} = \tau_{yx} = \mu \left(\frac{\partial u}{\partial y} + \frac{\partial v}{\partial x} \right) \tag{9}$$

where evaluation at the wall is performed to compute the wall shear stress. In the current finite element formulation, grid refinement is performed in the boundary layer region to accurately predict the velocity profile near the wall.

Once the near-wall velocity predictions are obtained, the wall shear stress, τ_w, is approximated based on the shape functions and Equation (9) as follows:

$$\tau_w \approx \mu \sum_{i=1}^{4} \frac{\partial N_i}{\partial y} \mathscr{U}_i + \mu \sum_{i=1}^{4} \frac{\partial N_i}{\partial x} \mathscr{V}_i \tag{10}$$

where $\mathscr{U}_i$ and $\mathscr{V}_i$ refer to nodal velocities at local node i. The shape functions, N_i, are evaluated within the boundary element at the local node co-ordinates corresponding to the node on the physical boundary. Then, integration of this wall shear stress, by summation of the integrated boundary terms along the entire surface area of the object, yields the frictional drag force.

In addition to these frictional forces, pressure drag arises due to pressure on the object. The total drag force, $\mathscr{D}$, is the sum of the friction and pressure drag. In fluid flow past a bluff body at high Reynolds numbers, separation of the boundary layer from the surface largely contributes to the pressure drag. In the present studies, the pressure drag is obtained

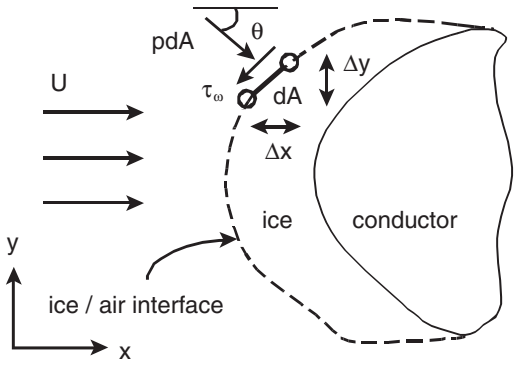

Figure 2. Pressure and shear forces on an arbitrary curved surface.

in a similar manner as the frictional drag, whereby the appropriate component of pressure is integrated along the surface area. This pressure component refers to the component of the pressure force, $p\,\mathrm{d}A$, acting normal to the boundary element area, $\mathrm{d}A$, in the direction of the upstream velocity (see Figure 2). For example, in the case of a fluid flow past a curved body in Figure 2, or more specifically, a discretized linear surface element along this body, the drag force, $\mathscr{D}$, is computed from

$$\mathscr{D} = \int_A p\,\cos(\theta)\,\mathrm{d}A + \int_A \tau_\mathrm{w}\,\sin(\theta)\,\mathrm{d}A \tag{11}$$

where

$$\cos(\theta) = \frac{\Delta y}{(\Delta x^2 + \Delta y^2)^{1/2}} \tag{12}$$

$$\sin(\theta) = \frac{\Delta x}{(\Delta x^2 + \Delta y^2)^{1/2}} \tag{13}$$

When computing the drag and lift forces, the pressure and shear stress are evaluated at the nodes along the physical boundary. For example, the area integrals in Equation (11) are subdivided into discrete parts representing the edges of boundary control volumes along the iced surface. The nodal pressure is multiplied by this surface area and $\cos(\theta)$, while the shear stress term requires velocities at surrounding nodes, as outlined in Equation (10).

Once the pressure and frictional drag forces are combined, the drag coefficient is obtained as

$$c_\mathrm{d} = \frac{\mathscr{D}}{(1/2)\rho V^2 A} \tag{14}$$

where V is the total velocity magnitude of the freestream fluid. In a similar way, the lift force, $\mathscr{L}$, and lift coefficient, c_l, are computed from

$$\mathscr{L} = -\int_A p\,\sin(\theta)\,\mathrm{d}A + \int_A \tau_\mathrm{w}\,\cos(\theta)\,\mathrm{d}A \tag{15}$$

$$c_l = \frac{\mathscr{L}}{(1/2)\rho V^2 A} \tag{16}$$

In this case, the resultant lift force, $\mathscr{L}$, is taken to be normal to the upstream velocity.

The skin friction drag represents the drag force on the body due to viscous shear stresses over the surface. On the other hand, pressure drag (or form drag) occurs due to the static pressure distribution around the body, acting in the direction of motion. It can be subdivided into forebody and rear (base) drag components. The relative contribution of friction and pressure drag largely depends on the shape of the surface. As the body thickness increases, the percentage of friction drag decreases. For example, for a thin flat plate, the drag force is 100% friction drag. But for a circular cylinder, the thickness is equal to the chord length and the friction drag is only about 3%, while the remaining 97% is pressure drag. Pressure drag largely involves flow separation, which mainly occurs on the downstream side of the iced and uniced conductors, so the drag and lift coefficients are considered to be dominated by base drag. Also, the magnitude of the pressure drag changes with Reynolds number, when the size of the low pressure wake region is reduced. For example, the pressure drag and resulting drag coefficient decrease due to delayed separation of the boundary layer and a narrower downstream wake for turbulent flow.

In view of the importance of base drag, the accuracy of the near-wall pressure field is significant when predicting the drag and lift coefficients. This observation emphasizes a primary purpose of this article to describe a more accurate pressure/velocity coupling through convection modelling when predicting those coefficients. Unlike previous upwind methods based on single variable interpolation (such as the upwind differencing scheme (UDS); see Appendix A), the next sub-section will outline a sub-element multi-variable link between pressure and velocity. This method is based on pressure weighted upwinding at the integration point. In this way, non-physical decouplings between problem variables can be prevented, such as a sudden near-wall pressure change having little or no effect on nearby velocities when the upwind interpolation excludes such links.

3.2. Pressure weighted upwinding in near-wall convection modelling

As indicated in the previous section, the numerical model requires accurate predictions of pressure and velocity near the wall when calculating the drag and lift forces. In this section, a procedure is outlined for the near-wall pressure/velocity coupling when predicting these forces, based on Schneider and Raw [6] and later extended to multiphase flows with droplets by Naterer [23]. Such extensions require separate evaluation of the upwind coefficients for the dispersed (droplet) and carrier (air) phases, as well as additional terms involving cross-phase interactions such as the interfacial drag between droplets and air. Freezing of impinging droplets on the surface establishes the shape of the iced cable, so convection modelling of both droplets and air have direct relevance to the cable drag problem.

Unlike conventional methods, which typically lack a pressure weighting in the convective upwinding (such as UDS [3]), the current approach includes all relevant physical mechanisms when calculating the upwinded velocities locally. In this way, a de-coupling of problem variables leading to the checkerboard problem [3] would not occur. The pressure weighted upwinding precludes a de-coupling between the integration point and nodal pressures leading to such problems, without requiring staggered grids. Also, it will be shown that this capability

can provide higher accuracy, in terms of integration point variables (see Appendix A) and predictions of the flow induced forces on iced surfaces (Section 3.3).

The control volume equation in Equation (7) is completed after all elements are assembled, since all sub-control-volume contributions to a conservation equation for a particular global node must be considered. However, it remains that the integration point values, such as integration point velocities, $\hat{u}_{\mathrm{ip1}}$ and $\hat{v}_{\mathrm{ip1}}$ in Equation (8), still have to be related to nodal variables, such as $\mathscr{U}_1$, $\mathscr{V}_1$ and $\mathscr{P}_1$, in order to provide a well-posed algebraic system. Both convecting and convected velocities are constructed in the same manner for the integration point velocities. However, as discussed earlier, linearized values from a previous iteration are used for the convected velocities, while the convecting velocities are active variables to be solved simultaneously in the mass and momentum equations. The following methods represent conventional methods for estimating $\hat{u}$ and $\hat{v}$ at the integration points.

UDS (*upwind differencing scheme*). The UDS approximation is $\hat{u}_{\mathrm{ip1}} = u_{\mathrm{u}}$ (at upstream point; see Figure 1). When the local flow direction is used to determine the upstream location, the method is also called the skew upwind differencing scheme (SUDS). This first-order upwinding neglects the influence of nodal pressure on the integration point velocity, which may lead to the non-physical de-coupling between problem variables. For example, a large pressure gradient between the upstream and integration points should affect the velocity field therein, but UDS does not include such connections with pressure.

CDS (*central differencing scheme*). In this scheme, linear interpolation between adjacent nodal values is used to calculate the integration point variable [3]. For example, in 1-D modelling of a general scalar quantity ϕ, this implies that $\phi_{i+1/2} = (\phi_i + \phi_{i+1})/2$, where i, $i+1$ and $i + 1/2$ refer to the west node, east node and integration point, respectively. In addition to neglecting pressure (as discussed for UDS), this method places an equal weighting on the downstream value, which lacks a physical basis, particularly for highly convective flows.

Hybrid schemes. Combinations of UDS, CDS and other schemes are called hybrid schemes. For example, the exponential differencing scheme (EDS) provides a balance between UDS and CDS based on the local grid Peclet number ($Pe = \rho \mathscr{U}_i \Delta x_i / \Gamma$, where Γ refers to a diffusion coefficient). This scheme gives a smooth transition from CDS in the diffusion limit ($Pe \to 0$) to UDS as $Pe \to \infty$. Other hybrid schemes can provide higher order accuracy, i.e. QUICK (quadratic upstream interpolation for convection kinetics; [11]). Unlike these methods, this article focuses on an alternative hybrid scheme based on pressure weighted upwinding (called PINS), which will be shown to have certain benefits when applied to flow induced force calculations.

As described earlier, the integration point value of $\hat{u}_{\mathrm{ip}}$ is required for closure of the control volume equation, since it is needed in the convection term of Equation (8). In the current approach, the integration point velocities are determined from a local balance of transport processes, including pressure, convection and diffusion. In particular, these velocities are obtained from the transport forms of the momentum equations, corresponding to Equations (3)–(4). In the x and y directions, respectively,

$$\rho \frac{\partial u}{\partial t} + \rho u \frac{\partial u}{\partial x} + \rho v \frac{\partial u}{\partial y} = -\frac{\partial p}{\partial x} + \mu \left(\frac{\partial^2 u}{\partial x^2} + \frac{\partial^2 u}{\partial y^2} \right) \tag{17}$$

$$\rho \frac{\partial v}{\partial t} + \rho u \frac{\partial v}{\partial x} + \rho v \frac{\partial v}{\partial y} = -\frac{\partial p}{\partial y} + \mu \left(\frac{\partial^2 v}{\partial x^2} + \frac{\partial^2 v}{\partial y^2} \right) \tag{18}$$

It can be observed that these equations involve five distinct operators: transient (first term), convection (second and third terms), pressure (fourth term), diffusion (fifth and sixth terms) and source terms (seventh term). The solution for each integration point velocity is obtained by a suitable discrete approximation of each of these operators. Then, once these operators are assembled together, the integration point values can be found in terms of nodal variables, and then substituted back into the control volume equations to obtain an algebraic system for the nodal variables alone. This type of change to nodal variables is also made in the conventional upwinding schemes, such as UDS, but without a multi-variable dependence including pressure.

For Equations (17)–(18), the transient term at the integration point is approximated by a backward difference. For example, at integration point 1,

$$\left.\frac{\partial \hat{u}}{\partial t}\right|_{\text{ip1}} \approx \frac{\hat{u}_{\text{ip1}}^{n+1} - \hat{u}_{\text{ip1}}^{n}}{\Delta t} \tag{19}$$

where the superscripts $n+1$ and n denote current and previous time levels, respectively.

The convection operator in Equation (17) at ip1 is approximated by an upstream difference as follows:

$$\rho u \frac{\partial u}{\partial x} + \rho v \frac{\partial u}{\partial y} = \rho V \left(\frac{\partial u}{\partial m}\right) \approx \rho V \left(\frac{\hat{u}_{\text{ip1}} - u_{\text{u}}}{L_{\text{c}}}\right) \tag{20}$$

where $V = \sqrt{u^2 + v^2}$ and m represent the fluid velocity magnitude and the local streamwise direction, respectively. Also, L_{c} is the convection length scale and u_{u} represents the upwind value of $\hat{u}_{\text{ip}}$ (see Figure 1). The direction of the line between $\hat{u}_{\text{ip1}}$ and u_{u} is defined by the local velocity components at these locations. Skew upwinding is used in the current scheme, so that the upstream value, u_{u}, is calculated by an interpolation upstream to the sub-volume edge, where the local streamline through the integration point intersects that edge. For example, if the line segment in the upwind direction intersects the quadrant edge between local nodes 2 and 3 (as in Figure 1),

$$u_{\text{u}} \approx \frac{a}{b}\,\mathscr{U}_2 + \left(1 - \frac{a}{b}\right)\mathscr{U}_3 \tag{21}$$

where the uppercase $\mathscr{U}$ denotes nodal values. The values a and b refer to coefficients corresponding to linear interpolation for u_{u} in terms of $\mathscr{U}_2$ and $\mathscr{U}_3$ along the intersected edge. This skew upwinding retains both the directional and strength influences of convection at the integration point. Skew upwinding errors due to upstream differencing are reduced, when compared to non-skewed schemes [24].

A novel feature of this hybrid scheme is the pressure weighting on $\hat{u}_{\text{ip}}$ and $\hat{v}_{\text{ip}}$ through Equations (17)–(18). In those equations, an approximation to the local pressure gradient is required. Shape functions are used for the following local interpolation, i.e. at ip1 for the x direction,

$$\left.\frac{\partial p}{\partial x}\right|_{\text{ip1}} = \sum_{i=1}^{4} \frac{\partial N_i}{\partial x}\,\mathscr{P}_i \tag{22}$$

where the uppercase $\mathscr{P}_i$ refers to nodal values of pressure. The pressure gradient in the y direction can be constructed in a similar fashion.

In Equations (17)–(18), the diffusion (Laplacian) operator is approximated by a central difference, i.e.

$$\left.\frac{\partial^2 u}{\partial x^2}+\frac{\partial^2 u}{\partial y^2}\right|_{\mathrm{ip1}} \approx \frac{1}{L_{\mathrm{d}}^2}\left(\sum_{j=1}^{4} N_j \mathscr{U}_j - \hat{u}_{\mathrm{ip}}\right) \tag{23}$$

where L_{d} is given by the following diffusion length scale:

$$L_{\mathrm{d}}^2 = \left(\frac{2}{\Delta x^2}+\frac{8}{3\Delta y^2}\right)^{-1} \tag{24}$$

It can be verified that this expression has the correct scaling properties of the Laplacian operator, and the correct limiting behaviour for steady diffusion problems involving no source terms.

Finally, local source terms can be evaluated by either direct substitution of the corresponding integration point values, or interpolation of nodal values in a similar fashion as the construction of the pressure gradient term. These operators are all assembled into Equations (17)–(18) and expressed through influence coefficient (IC) matrices. Then, a local matrix inversion is required to express the four integration point values (per element) in terms of nodal values alone. These inverted condensing coefficient (CC) matrices are used to calculate the integration point velocities, such as $\hat{u}_{\mathrm{ip}}$ in Equation (17), as follows:

$$\{\hat{u}\} = (CC^u)^{-1}[IC^{uu}]\{\mathscr{U}\} + (CC^u)^{-1}[IC^{up}]\{\mathscr{P}\} + (CC^u)^{-1}\{RS^u\} \tag{25}$$

The right side source vector, {RS}, and the coefficient matrices are

$$\{\mathrm{RS}_i^{up}\} = \frac{\rho \hat{u}_i^o}{\Delta t} \tag{26}$$

$$[\mathrm{IC}^{uu}] = \begin{pmatrix} \frac{\rho V_1 \xi(1-r)}{L_{\mathrm{c},1}} + \frac{\mu N_1}{L_{\mathrm{d},1}^2} & \frac{\rho V_1 \zeta(1-s)}{L_{\mathrm{c},1}} + \frac{\mu N_2}{L_{\mathrm{d},1}^2} & \frac{\mu N_3}{L_{\mathrm{d},1}^2} & \frac{\mu N_4}{L_{\mathrm{d},1}^2} \\ \frac{\mu N_1}{L_{\mathrm{d},2}^2} & \frac{\rho V_2 \xi(1-r)}{L_{\mathrm{c},2}} + \frac{\mu N_2}{L_{\mathrm{d},2}^2} & \frac{\rho V_2 \zeta(1-s)}{L_{\mathrm{c},2}} + \frac{\mu N_3}{L_{\mathrm{d},2}^2} & \frac{\mu N_4}{L_{\mathrm{d},2}^2} \\ \frac{\mu N_1}{L_{\mathrm{d},3}^2} & \frac{\mu N_2}{L_{\mathrm{d},3}^2} & \frac{\rho V_3 \zeta(1-s)}{L_{\mathrm{c},3}} + \frac{\mu N_3}{L_{\mathrm{d},3}^2} & \frac{\rho V_3 \xi(1-r)}{L_{\mathrm{c},3}} + \frac{\mu N_4}{L_{\mathrm{d},3}^2} \\ \frac{\rho V_4 \xi(1-r)}{L_{\mathrm{c},4}} + \frac{\mu N_1}{L_{\mathrm{d},4}^2} & \frac{\mu N_2}{L_{\mathrm{d},4}^2} & \frac{\mu N_3}{L_{\mathrm{d},4}^2} & \frac{\rho V_4 \zeta(1-s)}{L_{\mathrm{c},4}} + \frac{\mu N_4}{L_{\mathrm{d},4}^2} \end{pmatrix} \tag{27}$$

$$[\mathrm{IC}_{i,j}^{up}] = -\left.\frac{\partial N_i}{\partial x}\right|_j \tag{28}$$

$$[\mathrm{CC}^u] = \frac{\rho}{\Delta t} I_4 + \begin{pmatrix} \frac{\rho V_1}{L_{\mathrm{c},1}} + \frac{\mu}{L_{\mathrm{d},1}^2} & \frac{-\zeta s \rho V_1}{L_{\mathrm{c},1}} & 0 & \frac{-\xi r \rho V_1}{L_{\mathrm{c},1}} \\ \frac{-\xi r \rho V_2}{L_{\mathrm{c},2}} & \frac{\rho V_2}{L_{\mathrm{c},2}} + \frac{\mu}{L_{\mathrm{d},2}^2} & \frac{-\zeta s \rho V_2}{L_{\mathrm{c},2}} & 0 \\ 0 & \frac{-\zeta s \rho V_3}{L_{\mathrm{c},3}} & \frac{\rho V_3}{L_{\mathrm{c},3}} + \frac{\mu}{L_{\mathrm{d},3}^2} & \frac{-\xi r \rho V_3}{L_{\mathrm{c},3}} \\ \frac{-\zeta s \rho V_3}{L_{\mathrm{c},3}} & 0 & \frac{-\xi r \rho V_4}{L_{\mathrm{c},4}} & \frac{\rho V_4}{L_{\mathrm{c},4}} + \frac{\mu}{L_{\mathrm{d},4}^2} \end{pmatrix} \tag{29}$$

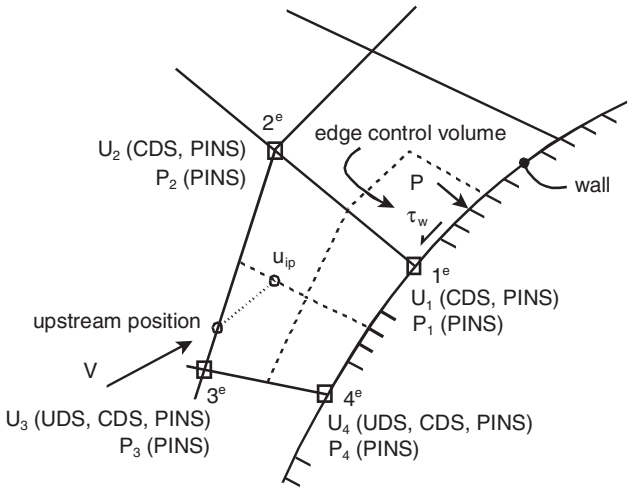

Figure 3. Convective upwinding for near-wall force calculations.

The 4×4 identity matrix is denoted by I_4. The numerical subscripts refer to the integration point numbers. Analogous coefficient matrices are obtained for the $\hat{v}_{ip}$ velocity in Equation (18).

In the previous equations, the coefficients ζ, ξ and r are used to represent the type of skewed upwinding. This upwinding involves interpolation of upstream values based on adjacent nodal and integration point values in the appropriate sub-element. For example, consider an upstream interpolation for $\hat{u}_{ip1}$ in SCV1 of Figure 1. Values of $\zeta = 1$, $\xi = 0$ or $\zeta = 0$, $\xi = 1$ represent two directions, depending on a negative or positive dot product between the outward sub-surface normal vector and local velocity, respectively. In our example when the upstream value of $\hat{u}_{ip1}$ intersects the sub-element edge of SCV2, the former values are used. Then, interpolation for the upstream value of $\hat{u}_{ip1}$ is taken between local node 2 and integration point 2 velocities, based on the geometric weighting factor s (note: factor r for flows in the opposite direction). This example describes a single case, while the range of ζ, ξ and r (or s) values includes other cases for different flow directions or interpolation variables. For example, the case of $\zeta = 0$, $\xi = 1$ represents flow from right to left in Figure 1. These coefficients are used to find $\hat{u}_{ip}$ in Equation (25), and similarly for $\hat{v}_{ip}$. Then, the convective terms in Equation (8) are obtained, so that the full control volume equations can be assembled and solved.

3.3. Improved accuracy of pressure weighted upwinding

In this section, it will be shown that the pressure weighted upwinding can improve the order of accuracy of the flow induced force calculations, as compared with past upwinding schemes such as UDS. Figure 3 illustrates an element along the wall, particularly focusing on the surrounding nodes and showing which variables are used in each type of upwinding scheme. It can be seen that PINS uses all nodal velocities and pressures within the element, whereas the other methods use some combination of variables, but not including pressure. The following order accuracy study will be presented, with reference to Figure 3 and a Taylor series analysis.

In Figure 3, an example is considered with upwinding of $\hat{u}_{ip}$ to an upstream location on the surface joining local nodes 2 and 3. For this example and the no-slip boundary conditions at the wall, Equation (10) becomes

$$\tau_w = \mu\left(\frac{\partial N_2}{\partial x}\mathscr{U}_2 + \frac{\partial N_3}{\partial x}\mathscr{U}_3\right) + \mu\left(\frac{\partial N_2}{\partial y}\mathscr{V}_2 + \frac{\partial N_3}{\partial y}\mathscr{V}_3\right) \tag{30}$$

The uppercase $\mathscr{U}$ and $\mathscr{V}$ refer to nodal velocities, and should be distinguished from V, which represents the total velocity magnitude in previous sections.

Using the chain rule of calculus to find the derivatives of the shape functions for Equation (30), and substituting $s = -1$ and $t = -1$ at local node 4 on the wall,

$$\tau_w = \frac{\mu}{4A}(a_{tu}\mathscr{U}_2 + (b_{tu} - a_{tu})\mathscr{U}_3) + \frac{\mu}{4A}(a_{tv}\mathscr{V}_2 + (b_{tv} - a_{tv})\mathscr{V}_3) \tag{31}$$

where

$$a_{tu} = y_3 - y_4 \tag{32}$$

$$b_{tu} = y_3 - y_2 \tag{33}$$

$$a_{tv} = x_4 - x_3 \tag{34}$$

$$b_{tv} = x_2 - x_3 \tag{35}$$

and A refers to the area of the element (Jacobian of transformation between local/global co-ordinates).

As mentioned earlier, the purpose of this section is to determine how the convective upwinding affects the accuracy of the previous wall shear stress and resulting force calculations. The steady state relationships will be established through a Taylor Series analysis of Equations (17)–(18). Equation (17) may be written as

$$\rho V\left(\frac{\partial u}{\partial m}\right) + \beta_u = 0 \tag{36}$$

where β_u includes the pressure gradient and diffusion terms. Also, differentiation of the convective term is written in the streamwise (m) direction. Using skew upwinding as described in Equation (20),

$$\rho V'\left(\frac{u'_{ip} - u'_u}{L}\right) + \beta'_u = 0 \tag{37}$$

where the prime notation refers to approximate (numerical) values. A similar result is obtained for the y-momentum equation.

For skewed upwinding from the integration point to sides 2–3, as indicated by Figure 3 and Equation (21), the result in Equation (37) can be written as

$$u'_{ip} + \left(\frac{L}{\rho V'}\right)\beta'_u = \frac{1}{b_{iu}}\{a_{iu}\mathscr{U}_2 + (b_{iu} - a_{iu})\mathscr{U}_3\} \tag{38}$$

Similarly for the y-momentum equation,

$$v'_{\mathrm{ip}} + \left(\frac{L}{\rho V'}\right)\beta'_v = \frac{1}{b_{iv}}\{a_{iv}\mathscr{V}_2 + (b_{iv} - a_{iv})\mathscr{V}_3\} \tag{39}$$

Based on a similarity of the right sides of Equations (31), (38) and (39), the wall shear stress and integration point velocities can be related.

The coefficients a_{iu}, a_{iv}, b_{iu} and b_{iv} refer to the interpolation coefficients, as discussed in Equation (21). From their definitions, b_{tv} and b_{iv} have orders of magnitude approximately equal to the side length, and it can be shown that

$$b_{iu}^2 = b_{tu}^2 + b_{tv}^2 \tag{40}$$

As a result, adding Equations (38) and (39) together, subtracting Equation (31), and then considering the order of magnitudes of the resulting terms,

$$\mathscr{O}\left\{b_{iu}u'_{\mathrm{ip}} + \left(\frac{Lb_{iu}}{\rho V'}\right)\beta'_{\mathrm{u}} + b_{iv}v'_{\mathrm{ip}} + \left(\frac{Lb_{iv}}{\rho V'}\right)\beta'_v\right\} = \mathscr{O}\left\{\frac{4A\tau_{\mathrm{w}}}{\mu}\right\} \tag{41}$$

Considering the shear stress portion of the drag force, $\mathscr{D}_{\mathrm{f}}$, and the corresponding integral in Equation (11), its order of magnitude (per unit depth of surface) can be approximated as

$$\mathscr{O}(\mathscr{D}_{\mathrm{f}}) = \mathscr{O}(\tau_{\mathrm{w}}\ \sin(\theta)L) \tag{42}$$

When this result is used in Equation (41), it can be shown that the order of accuracy of the frictional drag, $\mathscr{D}_{\mathrm{f}}$, and integration point velocities, u'_{ip} and v'_{ip}, become the same. When divided by $\rho V'^2 A/2$, the drag coefficient, c_{d}, is obtained. The area factor, A, in this calculation refers to the total surface area, so it is independent of the mesh spacing.

Also, the β'_{u} and β'_v terms in Equation (37) include the approximated pressure gradients. Once scaled and multiplied by the characteristic length scale, L, in Equation (41), the second and fourth terms of that equation become proportional to the total pressure, p'. Both the frictional drag, $\mathscr{D}_{\mathrm{f}}$, and pressure drag portion, $\mathscr{D}_{\mathrm{p}}$, contribute to the total drag force, $\mathscr{D}$, in Equation (11). The accuracy of the predicted drag force and corresponding drag coefficient, c_{d}, become equal to the order of accuracy of the integration point velocities, u'_{ip} and v'_{ip}.

For a conventional upwinding scheme such as UDS, a Taylor series expansion of u'_{ip} along the local streamline back to the upstream location, suggests that UDS and u'_{ip} are first-order accurate. This upstream location is determined at the intersection of the local streamline with the edge of the element. As a result, the drag coefficient becomes first-order, based on the previous discussion regarding the convection modelling and force calculations. However, it can be shown that PINS yields second-order accuracy in the integration point velocities (see Appendix A), and based on the previous analysis, also second-order accuracy in the drag coefficient. Thus, it is considered that the pressure weighted upwinding in near-wall elements, as described in Section 3.2, improves the order of accuracy of the predicted forces.

3.4. Special applicability to force predictions on iced surfaces

Although the previous near-wall upwinding method can be applied to force predictions for any general shape of surface, it exhibits special applicability to iced surfaces. Numerical predictions of flow and ice induced forces involve considerable difficulty due to the complex

physical phenomena at the interfacial boundary, i.e. impinging droplets, phase change heat transfer, flowing supercooled surface film, moving boundary, and so on. Due to the importance of near-wall convection in icing applications, and other applications involving many simultaneous interfacial processes (such as spray deposition manufacturing or droplet breakup on combustion chamber walls), highly accurate upwind methods are needed for the near-wall force predictions.

Furthermore, past numerical methods have often needed time-consuming steps to overcome the difficulties of predicting the interfacial processes. For example, re-meshing at each time step entails considerable CPU cost, particularly when near-wall grid refinement is needed for the boundary layer predictions. Further examples involving aircraft icing are documented by Cebeci and Chen [13], Hedde and Guffond [14], Shin *et al.* [15] and others. Recent advances have sought alternatives for overcoming these difficulties of icing predictions. Naterer [23] describes an Eulerian volume averaging approach, which precludes re-meshing at each time step by identifying the ice boundary through the local phase volume fractions of liquid, ice and air. The ice shape changes over time, without requiring re-meshing at the moving boundary of the ice surface.

Eulerian volume averaging allows coarser elements with reduced CPU cost, when compared against Lagrangian methods with tracking of individual droplet trajectories. But a single near-wall refinement of elements cannot be accommodated on the fixed grid, since the unknown position of the ice interface moves over time. As a result, highly accurate alternatives to conventional upwinding are needed to establish the pressure/velocity coupling at a sub-element level, when predicting the forces on the iced surface. Unlike other past methods discussed in the appendix, PINS provides such sub-element links between pressure and velocity.

4. EXPERIMENTAL VALIDATION OF PREDICTIVE MODEL

Experimental data was used for validation and verification of the predicted results. The measured data was collected in a closed loop wind tunnel in the Department of Mechanical and Industrial Engineering at the University of Manitoba. The air velocity ranged up to 36 m/s in the test section, whose dimensions are $0.53\,\text{m} \times 0.76\,\text{m}$, with a length of 1.83 m. A traversing mechanism was used in the wind tunnel with pressure probe measurements [25]. Aerodynamic forces associated with flow past various test pieces were obtained through measurements with a strain gauge balance (see Figure 4). The test pieces in this study include cables (i.e. stranded and smooth circular cylinders) under iced and uniced conditions. Actual iced cables were obtained separately from outdoor freezing rain experiments [26]. Following those experiments, plaster cast samples of the actual iced specimens were obtained, and then mounted and tested in the wind tunnel. Effects due to shrinkage of plaster casts from the iced samples, as well as differences in surface texture characteristics between samples, were considered to be negligible.

The aerodynamic forces were measured with a six-component strain gauge balance, which was connected to a transducer conditioner. Forces exerted by the flow in the wind tunnel were obtained from converted strain gauge signals, in conjunction with a digital voltmeter. Each test piece was mounted in the wind tunnel with couplings to fix the cable samples tightly between the test section walls. These couplings reduced any flow induced vibrations or leaked flow around the edges of a test specimen. Each test piece was mounted vertically on the strain gauge balance. The reference zero degree angle of attack was defined as the thickest point

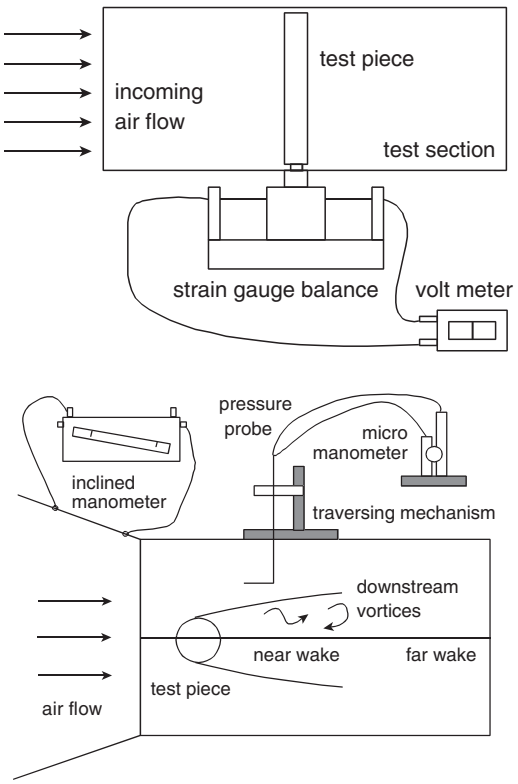

Figure 4. Experimental setup for validation of flow induced force calculations.

of ice formation, facing directly into the upstream direction. Preliminary testing of prismatic models with well known drag and lift coefficients (i.e. smooth cylinder and square sections) was performed for validation of the force measurements. Then, further testing of other iced and uniced conductors was performed over a range of Reynolds numbers.

In these experimental studies, the sources of error included limitations in the voltmeter accuracy itself. The electrical signals for the voltmeter of the strain gauge balance were measured within an accuracy of $\pm 0.05\,\mu V$. The measurements of drag and lift forces were based on strain gauge signals within an overall accuracy of approximately $\pm 2\,\mu V$. The corresponding accuracy in terms of force can be obtained through the appropriate conversion factors between force units and voltage units (i.e. $59\,\mu V \rightarrow 4.45\,N$ drag, $61\,\mu V \rightarrow 4.45\,N$ lift). In terms of the test pieces, their lengths and diameters were generally accurate to within about 0.2% of their reported values. For example, their lengths were 53.3 cm $\pm$ 1.0 mm. The diameter of the D-section (to be discussed in Section 5) was 6.3 cm $\pm$ 0.5 mm. Furthermore, in order to minimize errors arising from air infiltration through the mounting hole at the base of the test section, an air tight enclosure was constructed around the strain gauge balance. Based on measurements with and without the enclosure, it was observed that negligible errors occurred due to infiltration. Ranges of experimental uncertainties will be shown in upcoming figures in the following section.

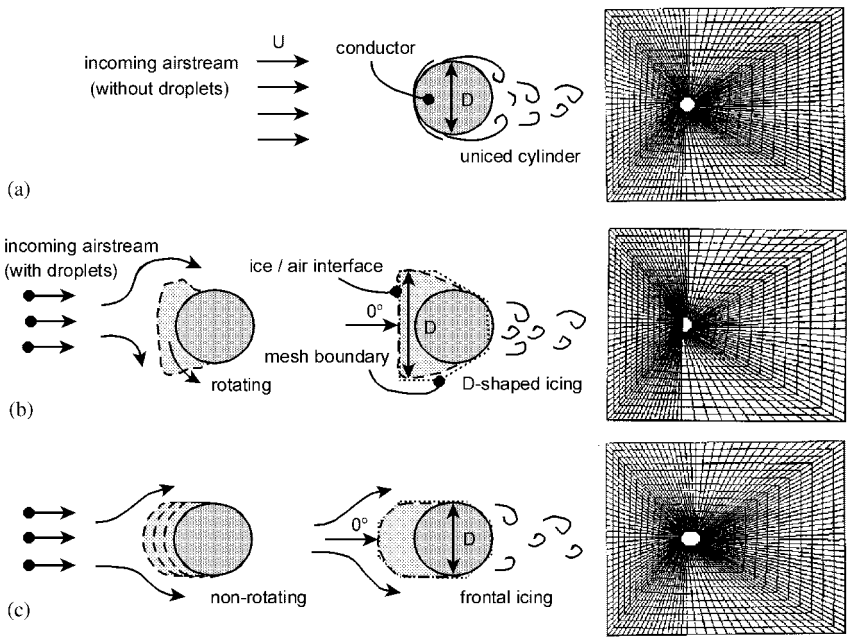

Figure 5. Flow configurations for (a) uniced, (b) D-shaped ice and (c) frontally iced cables.

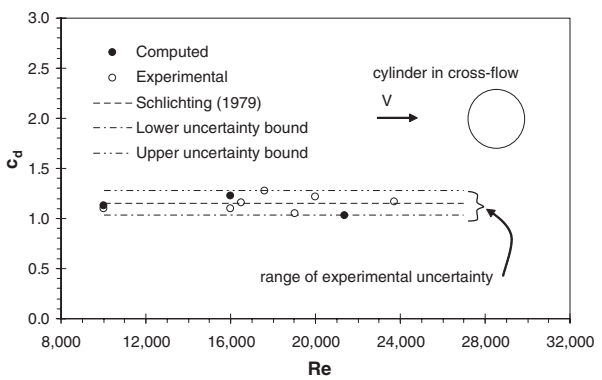

Figure 6. Effects of Reynolds number on drag coefficient (uniced cable).

5. RESULTS AND DISCUSSION

Results of predicted forces on uniced and iced cables will be presented in this section. The different types of cables, as well as sample mesh discretizations for each type of flow configuration, are shown in Figure 5. In Figures 5a and 6, fluid flow past an uniced cylindrical conductor is considered. In this example, the conductor diameter, D, is 3.43 cm, and the incoming air velocity, V, is 4.7 m/s. Several different mesh configurations were investigated,

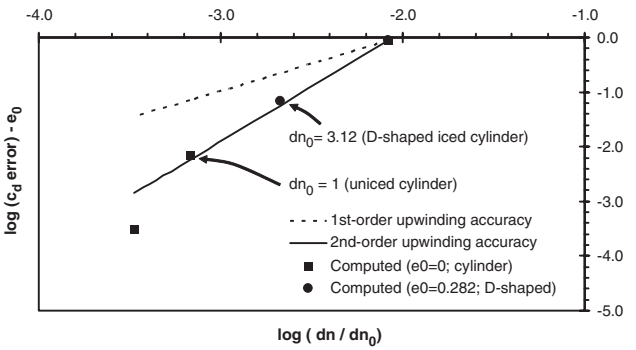

Figure 7. Grid refinement study (uniced cable).

including a 2193 node mesh (used for Figure 6), and grid refinement studies with 1921 nodes, 2193 nodes and other grids. The mesh spacing was refined within the boundary layer region of each mesh. The simulations involving this particular cable diameter correspond to a range of Reynolds numbers, Re (where $Re = VD/v$), between about 10^4 and 2.2×10^4. Along the cable surface, the boundary layer thickness increases in the streamwise direction, with a favorable (negative) pressure gradient along the upstream side of the cylinder. As the flow passes around the front edge to the downstream side, it experiences an adverse (positive) pressure gradient that leads to a swirling wake behind the cylinder. These processes affect the wall shear stress and pressure distributions, thereby influencing the aerodynamic forces exerted on the cylinder.

A comparison between the predicted results, experimental data and Fage and Warsap [27], presented by Schlichting [28, Figure 21.18] is shown in Figure 6. Periodic shedding of vortices renders the problem inherently unsteady, with slight temporal oscillations of c_d about a mean value. Instantaneous values of the drag coefficient are predicted once the numerical solution has converged, while the measured c_d values are averaged to find the time invariant average. The range of experimental uncertainty, based on measured and Schlichting's data, was considered to be about $\pm 10\%$. In the specified range of Reynolds number in Figure 6, the drag coefficient is nearly constant. In the numerical simulations, the surface of the cylinder was approximated by an 8-sided polygon. Although the curvature of the cylinder is not fully captured by an octagonal shape in the upcoming grid convergence studies, the results will be shown to converge to the proper range of measured data. As discussed earlier, the drag force is considered to be dominated by pressure drag, which largely involves flow separation on the downstream side of the cylinder. Since this entails base drag over the base area, it is not highly sensitive to the curvature of the surface. Furthermore, previous studies by Zhang [29] have confirmed that close agreement is reached between aerodynamic force coefficients, when comparing the flow past a circular cylinder and an octagon.

Grid refinement studies are shown in Figure 7. The horizontal axis refers to the logarithm of a non-dimensional grid spacing ratio along the outlet boundary. The grid spacing, dn, is non-dimensionalized with respect to the domain height. In order to properly compare trends for uniced (Figure 5(a)) and iced cables (Figure 5(b)), a reference grid spacing, dn_0, is used so each curve starts at the same initial point. A similar translation factor, e_0, is used in the

vertical axis, without affecting the main parameter of interest, namely the slope of each curve. The vertical axis shows the logarithm of the predicted drag coefficient error, as compared with measured data for the case of $Re = 10^4$. Plotting the results in a log–log form in Figure 7 is useful since the resulting slope can indicate the order accuracy of the numerical formulation. For the computed results in Figure 7, it can be observed that the logarithm of the solution error decreases with a slope of about 2 for the coarse grid refinement region in the upper right (i.e. approximately second-order accuracy). Second-order accuracy suggests that a reduction in grid spacing by a factor of 2, based on a characteristic dimension of importance, yields a reduction of solution error by a factor of about 4. A steeper slope reduction is observed for the finer grid region in the lower left. When the absolute errors lie within the range of experimental errors (described in previous section), this type of grid study may not be entirely conclusive with regards to detailed order accuracy. Also, even though convective upwinding is a major part of the model, it alone does not specify the order accuracy of the overall formulation. Nevertheless, it can be observed that the predicted error appears to be reduced when the grid spacing is smaller, and this reduction appears to be faster than first-order, when pressure weighted upwinding is used.

As discussed earlier, the flow past uniced and iced circular conductors is inherently unsteady, since vortices are shed periodically from the conductor. As a result, the value of the drag coefficient oscillates about a certain mean value. A regular oscillating pattern is typically established due to periodic vortex shedding behind a bluff body. In this article, the time averaged drag coefficients are reported in the measured data. More specifically, measurements were gathered by taking 10 values during the period of regular oscillations, and then arithmetically averaging them to determine the time invariant average. These measured values are compared against instantaneous computed drag coefficients, which vary by less than about $\pm 2\%$ from the time averaged value (i.e. cylinder in crossflow; [30]). Furthermore, such computed oscillations about the time invariant average generally remain well below the range of experimental uncertainty discussed earlier ($\pm 10\%$).

The time varying drag and lift coefficients are computed with first order temporal accuracy in Equation (7), unlike second order spatial accuracy (see Appendix A). However, this temporal order of accuracy is not considered to appreciably affect the time invariant averages or range of oscillations about the mean value, once the pattern of regular oscillations is established. Those features are characterized by the spatial variations of velocity and pressure throughout the flow field. The mean value becomes time independent, provided that a sufficient number of points is taken for the average and the remaining flow field has converged numerically. Second order temporal accuracy in the CVFEM can be established with a Crank–Nicolson scheme [22]. The higher temporal accuracy comes at the expense of certain disadvantages, such as storing property values at an intermediate time level, and storing values of the global stiffness matrix at the previous time level. Furthermore, once a regular oscillating pattern is established in the bluff body flow, predicting the time invariant average and range of oscillation about this average becomes more significant than a specific stage of vortex shedding in time.

A D-shaped cable (Figure 5(b)) can arise under a variety of atmospheric conditions with freezing precipitation and icing of cylindrical conductors. In conjunction with conductor rotation and a steady side wind, this shape can lead to unstable oscillations (galloping) of overhead power lines at certain angles of attack. Those cases would involve an incoming air stream at some angle with respect to the horizontal plane (see Figure 5(b)). When predicting the fluid–structure interactions leading to galloping, the flow-induced forces are needed. For

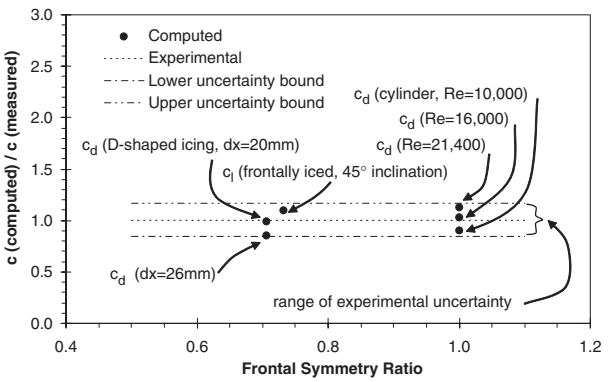

Figure 8. Predicted coefficients for D-shaped and frontally iced cables.

the D-shaped cable simulations (Figures 7, 8), the incoming air velocity is 15.2 m/s. The diameter at the midplane of the D-shaped cable is 6.3 cm. Various grid configurations were studied, including grids with 1649 nodes, 1921 nodes and others. These nodes were located essentially uniformly in the radial direction (outwards away from body), and the azimuthal direction (around the body). In this article, a stationary ice/air interface with a fixed grid is considered, so re-meshing at each time step due to impinging solidified droplets at the advancing ice interface is not performed. Even with a moving ice/air interface, this fixed grid approach can be used successfully [23].

The current formulation described in Section 3.2 exhibits certain advantages for handling the boundary conditions and sharp corners along the D-shaped surface. For example, the simultaneous pressure–velocity coupling within the near-wall elements effectively provides a sub-element refinement. Unlike other non-pressure based upwinding schemes (such as UDS, EDS, QUICK; see Appendix A), the current method links pressure with convective velocities at the four integration points within the near-wall element. This prevents any non-physical de-coupling between pressure and velocity therein, which would adversely affect the resulting force calculations. A higher flow resistance of the flat front edge of the body is encountered, when compared to the uniced cylinder. This flat edge leads to higher aerodynamic forces on the cable, and an upward lift force. Such forces are particularly evident at non-zero angles of attack, due to asymmetry in the direction normal to the incoming flow direction.

In Figure 7, the predicted results for the D-shaped cable approach the measured value of 2.61 when the grid spacing, dn, is refined. The grid spacing from the coarsest to finest mesh is reduced from 78 to 20 mm (outside of the boundary layer) in the horizontal direction along the horizontal midplane of the mesh. For the D-shaped cable, the computed drag coefficients generally oscillated between $\pm 6\%$ of the measured value, possibly due to periodic shedding of vortices behind the D-shaped body. A similar phenomenon was also observed in the measured data, whereby arithmetic averaging of several measurements was required to obtain a representative stationary value of the aerodynamic force.

When other results of drag coefficient for uniced and iced conductors were compared, the effects of D-shaped icing could be observed. As described earlier, the D-shape can occur due to conductor twisting with a steady side wind carrying droplets in icing conditions. Although

the drag coefficient for the uniced cylinder, $c_{d,u}$, remains nearly constant in Figure 6 at all angles of attack (due to self-symmetry), this coefficient varied with angle under D-shaped icing (coefficient denoted by $c_{d,d}$). At angles below about 40°, $c_{d,d}$ exceeds $c_{d,u}$ due to the larger bluff area exposed to the incoming airstream, as compared with the uniced cable. However, beyond those angles up to about 120°, an opposite trend ($c_{d,d} < c_{d,u}$) was observed. This trend is expected when the cross-stream width of the downstream separation zone is smaller, thereby creating a smaller low pressure wake behind the cable. Beyond about 120°, $c_{d,d}$ approaches $c_{d,u}$ since the shape exposed to the incoming airstream approaches the uniced cable shape. This suggested that the flow induced forces appear to be more affected by the ice-altered shapes on the upstream side, rather than the downstream side of the cable.

Another commonly encountered ice shape is illustrated in Figure 5(c), which occurs with an external flow past a cable with ice accretion into the direction of the incoming wind. The shape depicted in Figure 5(c) closely resembles iced cables documented by Poots [31]. Little or no ice accumulation on the downstream side of the cable indicates that the ice formation is likely rime (dry) ice. During rime ice buildup, impinging supercooled droplets freeze immediately upon impact on the upstream side, without runback of unfrozen water to the back side. Due to the elongation in the flow direction, together with asymmetry arising at non-zero angles of attack, considerable lift forces can be generated for these iced cables. Varying angles of attack can arise from twisting of the cable under its own weight, after the period of freezing precipitation.

In Figure 5(c), the accreted ice mass on the upstream side of the conductor, approximated by a series of line segments, represents the ice layers accumulated on the cylinder after a certain period of time. In this example, the incoming velocity is 27.9 m/s and the initially bare (uniced) cable diameter is 2.26 cm. A spatial discretization of 2193 nodes (2048 elements) was used with mesh refinement in the boundary layer. This particular discretization was determined to be an adequate mesh refinement, in view of the earlier grid sensitivity studies. By placing the body at different angles within the mesh, the effects of the angle of attack on the lift and drag forces could be investigated.

Figure 8 summarizes results for different iced and uniced configurations, including the previous frontally iced cable. The horizontal axis indicates the asymmetry, whereby the Frontal Symmetry Ratio, R, refers to the ratio of the radial body thicknesses at 0° and 45°. An uniced cylinder is completely symmetrical, with $R = 1$, while the D-shaped cable is least symmetrical about the axis of the incoming flow, and $R = 0.71$. On the vertical axis, the ratio between the computed and measured values of the aerodynamic coefficient is shown. For both c_d and c_l results, the predictions agree reasonably well with experimental data, when considering the range of experimental uncertainty of such data. The purpose of Figure 8 is to verify that the pressure weighted upwinding can be applied successfully to various geometrical configurations of iced cables. Due to complete symmetry of the uniced cylinder, the averaged lift coefficient is zero. However, this lift coefficient oscillates (positive and negative) over time about zero due to periodic shedding of vortices from the top and bottom (back) sides of the cable. As discussed earlier, it is the time averaged aerodynamic coefficients that are shown. Due to the symmetry, flow induced forces on uniced cables do not exhibit a dependence on the angle of attack, whereas frontal ice is asymmetric at different angles of attack, so angle-dependent variations occur.

A bluff body immersed in a fluid stream, such as air flowing past a circular conductor, is considered to be dynamically stable if its yawing motion due to the flow induced vibration is

damped out with time. In this case, the conductor's position tends to point into the general direction of the initial angle of attack. An overhead power line can be dynamically stable during early stages of ice buildup, but lose dynamical stability if the ice formation produces a certain shape, as the flowfield around the iced cable changes with time. The accumulated ice shape leads to time varying changes of drag and lift forces on the power lines, which can induce unstable line oscillations. Yu *et al*. [20, 32, 33] have presented three degrees-of-freedom modelling of such oscillations (galloping). Galloping is a high amplitude periodic oscillation arising from dynamic instability, which is caused by a steady crosswind acting on asymmetric iced cables. Such asymmetry generally appears when atmospheric conditions lead to ice buildup preferentially on the side of the cable facing the incoming wind and precipitation. Galloping represents dynamically unstable vibrations, which can lead to net forces much larger than forces on the cable arising from the ice weight alone. Actual frequencies of galloping usually vary between 0.15 and 1.0 Hz, depending on the oscillation mode excited. The amplitudes generally range between ± 0.1 and ± 1.0 times the sag of the span. Similarly, under certain atmospheric conditions with freezing precipitation, the onset of galloping can arise for D-shaped iced cables certain angles of attack [20, 32, 33].

Criteria for establishing the dynamical stability depend on the drag and lift coefficients, as well as their derivatives. For example, the Den Hartog condition for dynamical instability involves the derivative of lift coefficient with respect to angle relative to the incoming airflow [34]. This condition predicts a vertical instability of a power line, provided that the slope of the lift curve is positive (with an anti-clockwise positive reference) and its magnitude exceeds the drag coefficient. As a result, highly accurate methods are needed for calculating such slopes to determine the dynamical stability. Convection modelling and near-wall predictions of pressure and velocity are important components needed to achieve such accuracy. This article has described a pressure-weighted method of convective upwinding, which yields higher order accuracy than other past upwind methods (see Appendix). Furthermore, the sub-element link between pressure and velocity could prevent non-physical decouplings between these variables near the wall, as they may occur with sudden flow variations at different angles of attack. Variations of drag and lift forces with angle of attack are needed in the dynamical stability analysis, so these aspects of the convection modelling are considered to be important ways of accurately predicting the onset of instabilities such as galloping.

Other comparisons have been studied with stranded cables, smooth cylinders and octagonal cross-sections, in order to determine their effects on flow patterns and ice formation [25, 29]. It was observed that the effects of stranding and piecewise linear approximations of the circular conductor (i.e. octagon used in numerical simulations) were minor, provided that at least eight sides, or strands, are used to approximate the circular boundary. As a result, it is anticipated that the current numerical results can provide reasonable predictions of actual physical trends that would be encountered during icing of overhead power lines.

6. CONCLUSIONS

Convection modelling with pressure based upwinding is presented for predictions of flow induced forces on iced surfaces. A sub-element link between pressure and velocity is used for higher order accuracy, when calculating the near-wall shear stress and pressure distributions. Unlike other past methods of upwinding, the current method uses a pressure weighting

which can preclude a possible de-coupling between variables due to the pressure checkerboard problem. The numerical analysis is performed with a CVFEM (control-volume-based finite element method) for 2-D incompressible flows. Drag and lift coefficients are predicted for iced and uniced cables. Numerical results are successfully compared against experimental data collected in a closed loop wind tunnel with iced cable specimens.

APPENDIX A: ORDER ACCURACY COMPARISON OF DIFFERENT UPWIND SCHEMES

This appendix describes a baseline against which the current upwinding method (called PINS) can be compared. This baseline refers to the spatial order of accuracy of PINS, particularly when representing the integration point variable in terms of nodal values in the convective fluxes. It will be compared against other commonly used upwind schemes, namely UDS and EDS [3], as well as QUICK [11], in terms of order of accuracy and other features. These comparisons will be made for a common series of meshes, whereby the grid spacing of each mesh and the sequence of grid refinement are identical for each method. In this way, only the leading term of the Taylor series truncation analysis will be needed to compare each method's order of accuracy against the baseline method (PINS). Spatial interpolation with isoparametric, quadrilateral finite elements is used in the finite element procedure, independently of the type of convective upwinding. In the following analysis, a prime notation ($'$) will designate an inexact numerical value, while variables without this prime refer to exact values.

Consider that the local streamline intersects the volume edge between local nodes 2 and 3 (see Figure 1). Then, interpolation of the x-velocity component is performed between $\mathscr{U}_2$ and $\mathscr{U}_3$ when approximating the upwind value, u'_{u}, along that edge, i.e.

$$u'_{\mathrm{u}} = \left(\frac{a}{b}\right)\mathscr{U}_2 + \left(1 - \frac{a}{b}\right)\mathscr{U}_3 \tag{A1}$$

The parameter a refers to the distance between the upwind point and node 3 along edge 2–3, while b refers to the distance between nodes 2 and 3.

Performing a Taylor series expansion of nodal velocities about the upwind point along edge 2–3 (denoted by the normal direction, n),

$$\mathscr{U}_2 = u_{\mathrm{u}} + (b-a)\left(\frac{\partial u}{\partial n}\right) + \frac{1}{2}(b-a)^2\left(\frac{\partial^2 u}{\partial n^2}\right) + \mathscr{O}[(b-a)^3] \tag{A2}$$

$$\mathscr{U}_3 = u_{\mathrm{u}} - a\left(\frac{\partial u}{\partial n}\right) + \frac{1}{2}a^2\left(\frac{\partial^2 u}{\partial n^2}\right) + \mathscr{O}(a^3) \tag{A3}$$

Combining Equations (A1)–(A3),

$$u'_{\mathrm{u}} = u_{\mathrm{u}} + \mathscr{O}(b^2) \tag{A4}$$

Thus, the approximated upwind velocity, u'_{u}, can be expressed in terms of the exact upwind velocity, u_{u}, plus a second-order correction term.

Each integration point velocity obeys the transport form of momentum equation outlined in Equation (36), i.e.

$$\rho V\left(\frac{\partial u}{\partial m}\right)+\beta_{\mathrm{u}}=0 \tag{A5}$$

where m refers to the streamwise direction and β_{u} includes the pressure gradient, $\beta_{\mathrm{u,p}}$, and diffusion terms, $\beta_{\mathrm{u,u}}$. For the x-momentum equation,

$$\beta_{\mathrm{u}}=\beta_{\mathrm{u,p}}+\beta_{\mathrm{u,u}}=\frac{\partial p}{\partial x}-\mu\left(\frac{\partial^2 u}{\partial x^2}+\frac{\partial^2 u}{\partial y^2}\right) \tag{A6}$$

The following upwind schemes (PINS, UDS, EDS and QUICK) will be compared against each other, particularly regarding their accuracy in representing the actual transport processes outlined in Equation (A5).

A.1. PINS (physical influence scheme)

In this approach, the upwind velocity is determined after discretizing Equation (A4) in terms of the integration point velocity, u_{ip}, as follows:

$$\rho V'\left(\frac{u'_{\mathrm{ip}}-u'_{\mathrm{u}}}{L}\right)+\beta'_{\mathrm{u}}=0 \tag{A7}$$

A similar result is obtained for the y-momentum equation.

Re-arranging Equation (A7) and then substituting Equation (A4),

$$u'_{\mathrm{ip}}=u_{\mathrm{u}}-\frac{\beta'_{\mathrm{u}}L}{\rho V'}+\mathcal{O}(b^2) \tag{A8}$$

Assuming that the terms β'_{u} and V' are at least first-order accurate, then the third term can be expanded in terms of exact values as follows:

$$\frac{L(\beta_{\mathrm{u}}+\mathcal{O}(L))}{\rho(V+\mathcal{O}(L))}=\frac{L\beta_{\mathrm{u}}}{\rho V}+\frac{\mathcal{O}(L^2)}{\rho V+\rho\mathcal{O}(L)}-\frac{L\beta_{\mathrm{u}}\mathcal{O}(L)}{V(\rho V+\rho\mathcal{O}(L))} \tag{A9}$$

If the velocity, V, is further expressed in terms of the length scale, L, divided by a characteristic time scale, T, it can be shown that the first term on the right side becomes dominant when the grid spacing is reduced. In that case, Equation (A8) becomes

$$u'_{\mathrm{ip}}=u_{\mathrm{u}}-\frac{\beta_{\mathrm{u}}L}{\rho V}+\mathcal{O}(b^2) \tag{A10}$$

Applying a Taylor series expansion for the upwind velocity in the streamwise direction,

$$u_{\mathrm{u}}=u_{\mathrm{ip}}-L\left(\frac{\partial u}{\partial m}\right)_{\mathrm{ip}}+\frac{L^2}{2}\left(\frac{\partial^2 u}{\partial m^2}\right)_{\mathrm{ip}}+\mathcal{O}(L^3) \tag{A11}$$

Thus, comparing with Equation (A5),

$$u_{\mathrm{ip}}=u_{\mathrm{u}}-\frac{L\beta_{\mathrm{u}}}{\rho V}+\mathcal{O}(L^2) \tag{A12}$$

Comparing this exact value of the integration point velocity with the approximated value in Equation (A10),

$$u'_{\mathrm{ip}} = u_{\mathrm{ip}} + \mathcal{O}(b^2) + \mathcal{O}(L^2) \tag{A13}$$

Thus, upwinding based on PINS yields second-order accuracy of the integration point velocity, when calculating the convective fluxes at the edge of each control volume.

A.2. UDS (upwind differencing scheme)

In this method, pressure, diffusion and source terms are neglected, so Equation (A5) is approximated as follows:

$$\rho V' \left(\frac{u'_{\mathrm{ip}} - u'_{\mathrm{u}}}{L} \right) = 0 \tag{A14}$$

and similarly for the y-momentum equation. After re-arranging Equation (A14), it can be observed that the integration point velocity is approximated directly by the upwind velocity. However, from Equation (A11),

$$u_{\mathrm{u}} = u_{\mathrm{ip}} + \mathcal{O}(L) \tag{A15}$$

which suggests that this approximation of the integration point velocity is first-order accurate.

Thus, in addition to exhibiting a lower order accuracy than PINS, the velocity becomes de-coupled from pressure at the integration point in UDS. Such de-couplings may permit unrealistic local variations of velocity and pressure. For example, a large sub-element pressure gradient could arise around a sharp corner on the ice surface, without having any effect on the integration point velocity in Equation (A14), thereby destabilizing the computations. As a result, lower order accuracy and certain concerns regarding numerical stability are observed in UDS, when compared against PINS.

A.3. EDS (exponential differencing scheme)

Unlike UDS, this approach attempts to balance upstream and downstream nodal influences on the integration point velocity, based on the local grid Peclet number ($Pe = \rho \mathscr{U}_i \Delta x_i / \Gamma$, where Γ is the diffusion coefficient). Similarly as PINS, Equation (A5) is solved locally for the integration point velocity. But in contrast to PINS, β_{u} includes only diffusion terms, $\beta_{\mathrm{u,u}}$, and not the implicitly linked pressure field outlined in PINS, $\beta_{\mathrm{u,p}}$, i.e.

$$\beta_{\mathrm{u}} = \beta_{\mathrm{u,u}} = -\mu \left(\frac{\partial^2 u}{\partial x^2} + \frac{\partial^2 u}{\partial y^2} \right) \tag{A16}$$

For illustration purposes, consider a 1-D analytical solution of Equation (A5), while neglecting pressure and source terms in β_{u}, but including the diffusion component. For incompressible, viscous flow of a Newtonian fluid, this diffusion component in the x-momentum equation becomes the Laplacian of u_{ip}. The west node, integration point and east node are designated by subscripts W, ip and E, respectively. Solving Equation (A5) subject to known (specified) values of $\mathscr{U}$ at the nodes, and then evaluating the velocity at the integration point

based on this solution,

$$u_{\mathrm{ip}} = \left(\frac{1+\alpha}{2}\right)\mathscr{U}_{\mathrm{W}} + \left(\frac{1-\alpha}{2}\right)\mathscr{U}_{\mathrm{E}} \tag{A17}$$

where

$$\alpha = 1 - \frac{2(\mathrm{e}^{Pe/2} - 1)}{\mathrm{e}^{Pe} - 1} \tag{A18}$$

This approach allows the upwinded velocity to accommodate the proper upstream and downstream influences of adjacent nodal velocities. For example, the weighting on the upstream value increases when Pe increases (as expected).

Then, in terms of order accuracy, Equation (A8) becomes

$$u'_{\mathrm{ip}} = u_{\mathrm{u}} - \frac{\beta'_{\mathrm{u,u}} L}{\rho V'} + \mathscr{O}(b^2) \tag{A19}$$

and the exact value in Equation (A12) becomes

$$u_{\mathrm{ip}} = u_{\mathrm{u}} - \frac{L(\beta_{\mathrm{u,p}} + \beta_{\mathrm{u,u}})}{\rho V} + \mathscr{O}(L^2) \tag{A20}$$

As a result, comparing Equations (A19)–(A20),

$$u'_{\mathrm{ip}} = u_{\mathrm{ip}} + \frac{L\beta_{\mathrm{u,p}}}{\rho V} + \mathscr{O}(b^2) + \mathscr{O}(L^2) \tag{A21}$$

When Equation (A21) is compared against the analogous result in Equation (A13), it can be observed that the accuracy of the integration point variable in EDS becomes dependent on an additional pressure gradient term, $\beta_{\mathrm{u,p}}$. Based on the characteristic time and length introduced before Equation (A10), and the first order accuracy assumption leading to Equation (A9), the additional pressure term leads to first order accuracy in Equation (A21). Also, the method of EDS usually requires additional approximations to reduce the computational expense of calculating the exponential terms in Equation (A18) for the weighting factor, α (Minkowycz *et al.*, 1988).

A.4. QUICK (Quadratic upstream interpolation for convection kinetics)

A quadratic function is used for interpolation of integration point values in this approach, but the β_{u} term in Equation (A5) is neglected, similarly as UDS and EDS. Although higher order accuracy is achieved with this quadratic upstream interpolation, an analogous result of Equation (A21) is obtained. In this result, the pressure and diffusion terms yield first order accuracy when the upwind method is compared against the actual transport processes at the integration point. These actual processes require a momentum balance involving convection, pressure and diffusion terms, which cannot be fully realized with a conventional Taylor series analysis based on a single dependent variable, without the sub-element link between the integration point velocity and pressure.

APPENDIX B: NOMENCLATURE

a, b	interpolation coefficients
A	area
c_d	drag coefficient
c_l	lift coefficient
$\mathscr{D}$	drag force
D	diameter
L	length scale
$\mathscr{L}$	lift force
m	streamwise direction
N_i	bilinear shape function
p	kinematic pressure
$\mathscr{P}_i$	nodal pressure (local node i)
S	source term
s	local co-ordinate
t	time
$\mathscr{U}_i$	nodal x-velocity (local node i)
V	total velocity magnitude
$\mathscr{V}_i$	nodal y-velocity (local node i)
u, v	x, y-velocity components
x, y	global co-ordinates

Greek letters

β	pressure, diffusion terms
μ	dynamic viscosity
ϕ	general scalar variable
ρ	density
τ	shear stress
ξ	upwinding coefficient
ζ	upwinding coefficient

Subscripts

c	convection
d	diffusion
i	node i
ip	integration point
u	upwind
w	wall
x, y	co-ordinate directions

Superscripts

$n+1$	current time level
u	x-momentum equation

v y-momentum equation
p continuity equation

ACKNOWLEDGEMENTS

Financial support from Manitoba Hydro, and the assistance and insight provided by Dr. N. Popplewell (University of Manitoba) and Mr. J. Chan (Manitoba Hydro), are appreciated. Also, financial support from the Natural Sciences and Engineering Research Council of Canada is gratefully acknowledged.

REFERENCES

1. Canadian Electrical Code. Overhead systems and underground systems. *CSA Standard C22.3*, No. 1-M, 1979.
2. Gresho PM, Lee RL, Upson CD. FEM solution of the Navier–Stokes equations for vortex shedding behind a cylinder: experiments with the four-node element. *Advances in Water Resources* 1981; **4**:175–184.
3. Patankar SV. *Numerical Heat Transfer and Fluid Flow*. Hemisphere: Washington, DC, 1980.
4. Naterer GF. Sub-grid volumetric quadrature accuracy for transient compressible flow predictions. *International Journal for Numerical Methods in Fluids* 1997; **25**(2):143–149.
5. Minkowycz WJ, Sparrow EM, Schneider GE, Pletcher RH. *Handbook of Numerical Heat Transfer*. Wiley: New York, 1988.
6. Schneider GE, Raw MJ. Control-volume finite-element method for heat transfer and fluid flow using co-located variables—1. computational procedure. *Numerical Heat Transfer* 1987; **11**:363–390.
7. Wong HH, Raithby GD. Improved finite difference methods based on a critical evaluation of approximation errors. *Numerical Heat Transfer* 1979; **2**:139–163.
8. Van Doormaal JP, Turan A, Raithby GD. Evaluation of techniques for the calculation of internal recirculating flows. *AIAA Paper 87-0059*, AIAA 25th Aerospace Sciences Meeting, Reno, NV, 1987.
9. Lillington JN. A vector upstream differencing scheme for problems in fluid flow involving significant source terms in steady-state linear systems. *International Journal for Numerical Methods in Fluids* 1981; **1**:3–16.
10. Naterer GF. Constructing an entropy-stable upwind scheme for compressible fluid flow computations. *AIAA Journal* 1999; **37**(3):303–312.
11. Leonard BP. A stable and accurate convective modelling procedure based on quadratic upstream interpolation. *Computer Methods in Applied Mechanics and Engineering* 1979; **19**:59–98.
12. Hutchinson BR, Raithby GD. A multigrid method based on the additive correction strategy. *Numerical Heat Transfer* 1986; **9**:511–537.
13. Cebeci T, Chen H, Alemadaroglu N. Fortified LEWICE with viscous Effects. *AIAA Journal of Aircraft* 1991; **28**(9):564–571.
14. Hedde T, Guffond D. Development of a three-dimensional icing code, comparison with experimental shapes. *AIAA Paper 92-0041*, AIAA 30th Aerospace Sciences Meeting and Exhibit, January 6–9, Reno, NV, 1992.
15. Shin J, Berkowitz B, Chen HH, Cebeci T. Prediction of ice shapes and their effect on airfoil drag. *AIAA Journal of Aircraft* 1994; **31**(2):263–270.
16. Pinol S, Grau FX. Influence of the no-slip boundary condition on the prediction of drag, lift and heat transfer coefficients in the flow past a 2-D cylinder. *Numerical Heat Transfer A* 1998; **34**:313–330.
17. Fox RW, McDonald AT. *Introduction to Fluid Mechanics* (4th Edn). Wiley: New York, 1992.
18. Gharib MR, Shiels DG, Gharib M, Leonard A, Roshko A. Exploration of flow induced vibration at low mass and damping, *ASME 4th International Symposium on Fluid-Structure Interaction*, *Aeroelasticity*, *Flow Induced Vibration and Noise*, Dallas, TX, 1997.
19. Naterer GF, Rinn D. Towards entropy detection of anomalous mass and momentum exchange in incompressible fluid flow. *International Journal for Numerical Methods in Fluids* 2002; **39**(11):1013–1036.
20. Yu P, Desai YM, Popplewell N, Shah AH. *Modelling of Conductor Galloping*, vol. I and II, Manitoba Hydro, also prepared for the Canadian Electrical Association (No. 321 T 672): Montreal, Canada, August, 1992.
21. Naterer GF, Deng H, Popplewell N. Predicting and reducing glaze ice accretion on electric power lines with joule heating: theory and experiments. *CSME Transactions* 1999a; **23**(1A):51–70.
22. Naterer GF. *Heat Transfer in Single and Multiphase Systems*. CRC Press: Boca Raton, FL, 2002.
23. Naterer GF. Multiphase flow with impinging droplets and airstream interaction at a moving gas/solid interface. *International Journal of Multiphase Flow* 2002; **28**(3):451–477.
24. Raithby GD. Skew upstream differencing schemes for problems involving fluid flow. *Computer Methods in Applied Mechanics and Engineering* 1976; **9**:153–164.
25. Stumpf P. Determination of aerodynamic forces for iced single and twin-bundled conductors. *M.Sc. Thesis*, Department of Mechanical and Industrial Engineering, University of Manitoba, 1994.

26. Lu ML, Popplewell N, Shah AH, Barrett W, Au A. Mass of ice accretion from freezing rain simulations. *Proceedings*, *8th IWAIS*, Reykjavik, Iceland, 1998.
27. Fage A, Warsap J. The effects of turbulence and surface roughness on the drag of circular cylinders. British Aeronautical Research Council, *Reports and Memoranda*, *No. 1283*, London, 1930.
28. Schlichting H. *Boundary Layer Theory* (7th Edn). McGraw-Hill: New York, 1979.
29. Zhang C. A curved beam element and its application to traffic poles. *M.Sc. Thesis*, Department of Mechanical and Industrial Engineering, University of Manitoba, 1998.
30. Braza M, Chassaing P, Ha Minh H. Numerical study and physical analysis of the pressure and velocity fields in the near wake of a circular cylinder. *Journal of Fluid Mechanics* 1986; **165**:79–130.
31. Poots G. *Ice and Snow Accretion on Structures*. Research Studies Press Ltd.: Taunton, England, 1996.
32. Yu P, Desai YM, Shah AH, Popplewell N. Three degrees of freedom model for galloping, Part I: formulation. *ASCE Journal of Engineering Mechanics* 1993; **119**(12):2404–2425.
33. Yu P, Desai YM, Shah AH, Popplewell N. Three degrees of freedom model for galloping, Part I: solutions. *ASCE Journal of Engineering Mechanics* 1993; **119**(12):2426–2448.
34. Den Hartog JP. *Mechanical Vibrations*. McGraw-Hill: New York, 1956.

